

UAVSAR Polarimetric Calibration *

Alex Fore , Bruce Chapman , Scott Hensley , Thierry Michel , Ron Muellerschoen †

June 4, 2009

1 Introduction

Our calibration methodology is to perform radiometric and phase calibration within the processor and to perform cross-talk calibration as a (optional) stand-alone process. The parameters needed to perform radiometric and phase calibration are generally known a-priori, and we specify the calibration parameters using calibration files. A table of the calibration parameters is available at <http://uavsar.jpl.nasa.gov/data/cal/caltable.htm>.

2 Radiometric and Phase Calibration

In this Section we describe how we estimate and apply the radiometric and phase calibration parameters tabulated at <http://uavsar.jpl.nasa.gov/data/cal/caltable.htm>. Suppose we measure some polarimetric quantity, whose real scattering matrix is given by \mathcal{S} . After correcting for the antenna pattern (see Appendix (B)), and neglecting cross-talk we measure [6]

$$\mathcal{S}' = A \begin{bmatrix} s_{vv}f^2 \exp i(\phi_{t,v} + \phi_{r,v}) & s_{vh}(f/g) \exp i(\phi_{t,h} + \phi_{r,v}) \\ s_{hv}fg \exp i(\phi_{t,v} + \phi_{r,h}) & s_{hh} \exp i(\phi_{t,h} + \phi_{r,h}) \end{bmatrix}. \quad (1)$$

Here, A is the absolute calibration error (real number), f is the co-pol channel imbalance, g is the cross-pol channel imbalance, $\phi_{t,v}$ is the phase error incurred when transmitting v-pol, $\phi_{r,v}$ is the phase error incurred when receiving v-pol with similar definitions for h-pol. We may remove an arbitrary phase from this expression and we obtain

$$\mathcal{S}' = A \begin{bmatrix} s_{vv}f^2 \exp i(\phi_t + \phi_r) & s_{vh}(f/g) \exp i\phi_r \\ s_{hv}fg \exp i\phi_t & s_{hh} \end{bmatrix}, \quad (2)$$

where $\phi_t := \phi_{t,v} - \phi_{t,h}$, and $\phi_r := \phi_{r,v} - \phi_{r,h}$.

2.1 Estimation of Calibration Parameters

We now outline how we estimate parameters ϕ_t , ϕ_r , A , and f using corner reflectors and distributed targets. At a trihedral corner reflector, we expect the scattering matrix to be of the form $\mathcal{S}_{tri} = \sqrt{\sigma_{cr}} \begin{bmatrix} 1 & 0 \\ 0 & 1 \end{bmatrix}$, where σ_{cr} is given by Eq. (13). Then the observed scattered matrix at the corner reflectors has the form

$$\mathcal{S}'_{cr} = \begin{bmatrix} s'_{vv} & s'_{vh} \\ s'_{hv} & s'_{hh} \end{bmatrix} = A\sqrt{\sigma_{cr}} \begin{bmatrix} f^2 \exp i(\phi_t + \phi_r) & 0 \\ 0 & 1 \end{bmatrix}. \quad (3)$$

*This work was performed under contract with the National Aeronautics and Space Administration at the Jet Propulsion Laboratory, California Institute of Technology.

†The authors are with the Jet Propulsion Laboratory, California Institute of Technology. 4800 Oak Grove Dr., Pasadena. CA 91109.

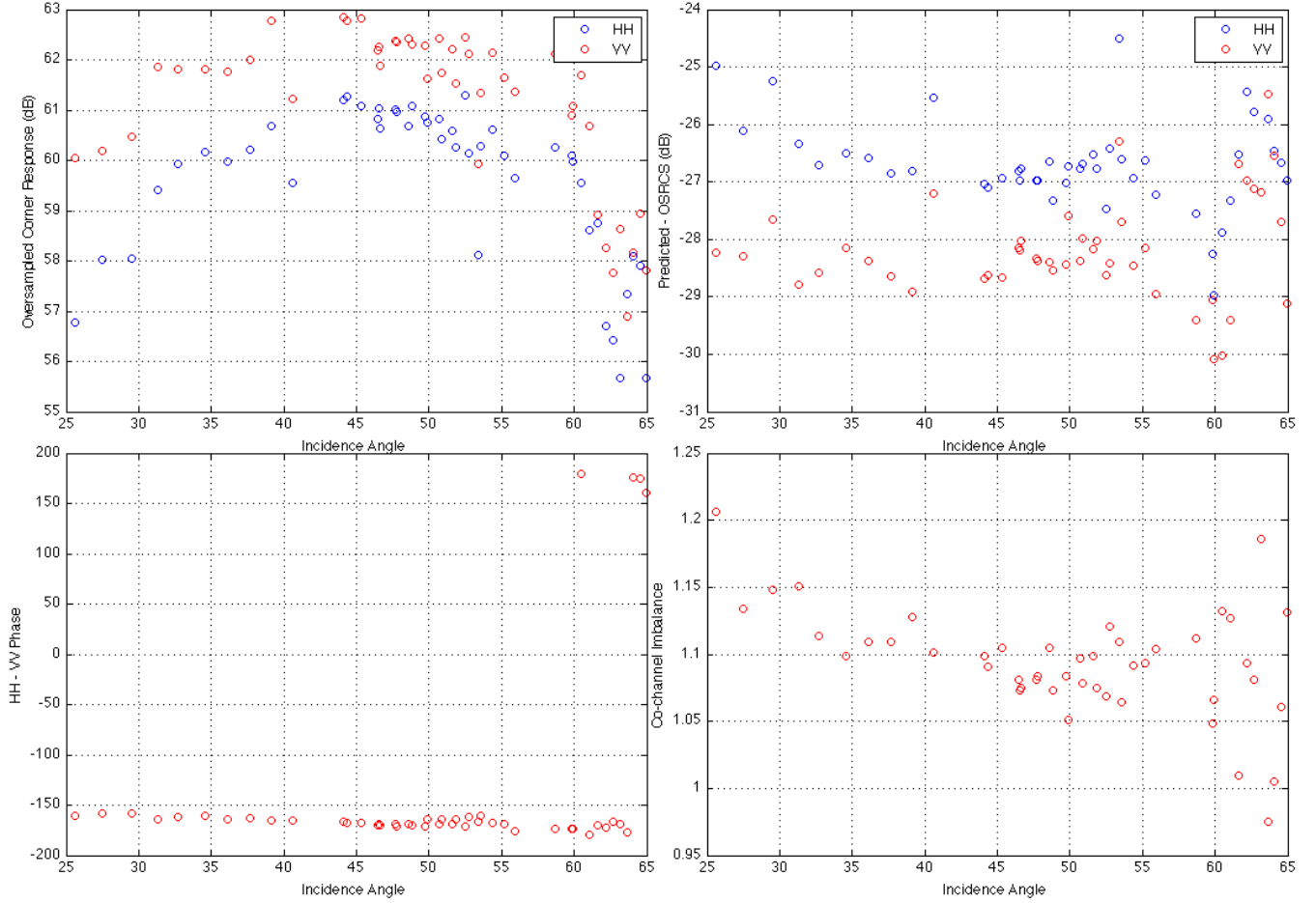


Figure 1: Example of data taken over the Rosamond corner reflector array, from which we estimate the radiometric and phase calibration parameters. We plot the over-sampled corner reflector response [dB] (top left), absolute calibration error [dB] (top right), the hh to vv phase bias (bottom left), and co-channel imbalance (bottom right). This data is used to estimate the quantities A , ϕ_{hh-vv} , and f .

As an example, we consider the data shown in Figure (1) – this data has only been calibrated for the antenna pattern. In this figure we plot the over-sampled corner responses $s'_{hh} s'^*_{hh}$ and $s'_{vv} s'^*_{vv}$ in the top left plot, the predicted RCS from Eq. (13) minus the over-sampled responses in the top right plot, the measured phase bias of the HH channel relative to the VV channel in the bottom left plot, and the co-channel imbalance in the bottom right plot. In Figure (2) we plot a few polarization signatures from the Rosamond corner reflector array from uncalibrated data. In Figure (3) we show the polarization signatures from the same data after calibration.

2.1.1 Absolute Calibration

To estimate the absolute calibration, A , from this data we consider the predicted-measured RCS shown in the upper right plot of Figure (1). We compute the average offset between the predicted RCS and the measured RCS and solve for A using the relationship $10 \log_{10} \left[\sigma_{cr} / \left(s'_{hh} s'^*_{hh} \right) \right] = -10 \log_{10} A^2$ obtained from Eq. (3).

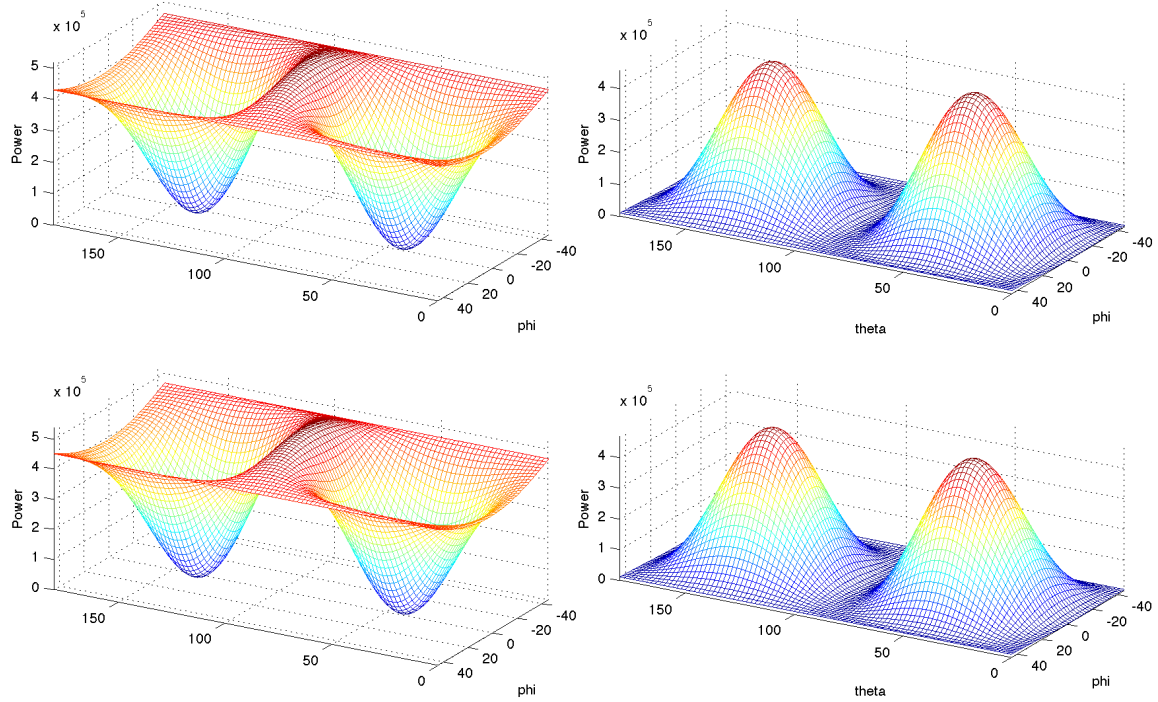


Figure 2: Polarization signatures of trihedral corner reflectors before any calibration is applied.

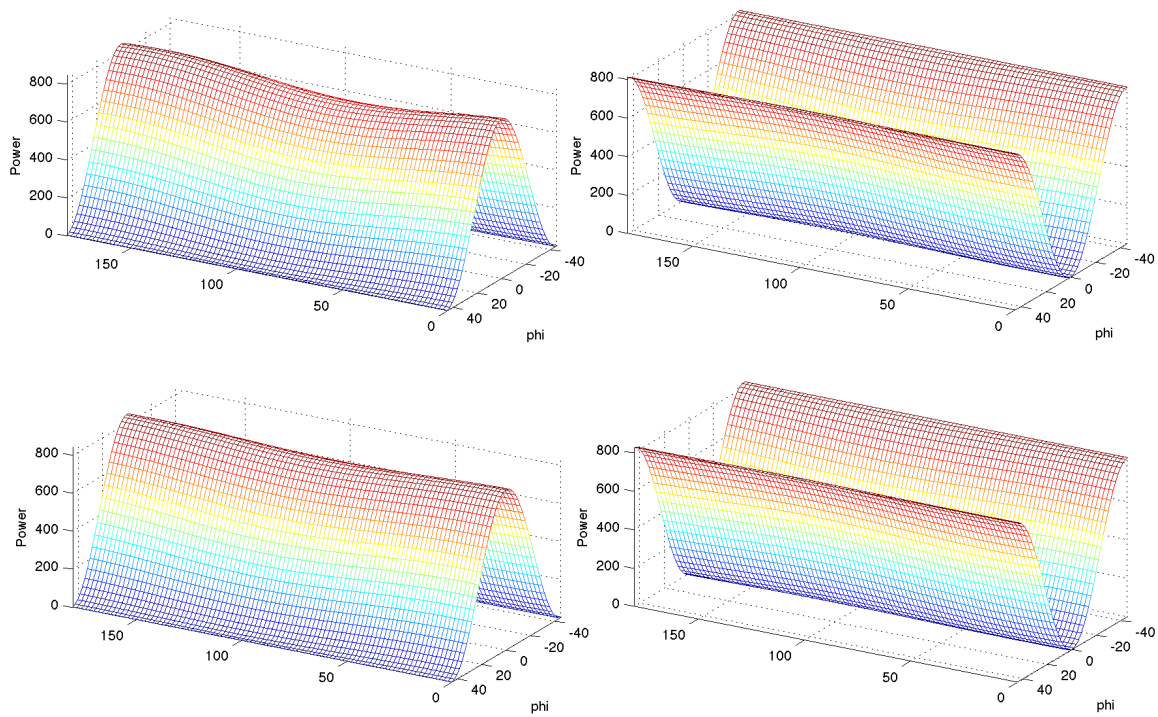


Figure 3: Polarization signatures of same trihedral corner reflectors after radiometric and phase calibration.

2.1.2 Channel Imbalances

Eq. (3) also show us that at a corner reflector the quantity $\left[s'_{vv} s'_{vv*} / \left(s'_{hh} s'_{hh*} \right) \right]^{0.25}$ is an estimate for f , the co-channel imbalance. In the bottom right of Figure (1) we plot an example of the observed co-channel imbalance as a function of incidence angle. From this data we can estimate f as the average of the observed co-pol channel imbalances over all the data points.

To determine the cross-pol channel imbalance, we compute the average hv and vh power over a large number of pixels. From equation Eq. (3) we can estimate the cross-pol imbalance as $g = \left[\langle |S'_{hv}|^2 \rangle / \langle |S'_{vh}|^2 \rangle \right]^{1/4}$.

2.1.3 Phase Bias

Again from Eq. (3) we expect that the quantity $\arg(s'_{vv} s'_{hh*})$ evaluated at a corner reflector is an estimate for $\phi_t + \phi_r$. We plot this data in the bottom left of Figure (1) and we observe a linear trend of this phase with incidence angle. We perform a least-squares fit of the model: $\phi_t + \phi_r = a_{\phi_t + \phi_r} + b_{\phi_t + \phi_r} (\theta_{inc} - 45 \text{ deg})$ to the data to obtain an estimate of $\phi_t + \phi_r$ as a function of incidence angle.

However we still need an estimate for $\phi_t - \phi_r$ to complete the phase calibration. From reciprocity we expect $s_{hv} = s_{vh}$, thus we can estimate the phase bias as $\phi_t - \phi_r = \arg(\langle s'_{hv} s'_{vh*} \rangle)$ over a large number of pixels, where $\langle \cdot \rangle$ indicates a coherent average.

2.2 Relation to Parameters in Table

The radiometric and phase calibration parameters listed at <http://uavsar.jpl.nasa.gov/data/cal/caltable.htm> are related to the parameters derived as in the following table

Sigma Nought Bias HH LRTI80	$1/A$
Sigma Nought Bias HV LRTI80	$1/(Afg)$
Sigma Nought Bias VH LRTI80	$g/(Af)$
Sigma Nought Bias VV LRTI80	$1/(Af^2)$
HH-VV Phase Bias LRTI80	$a_{\phi_t + \phi_r}$
HV-VH Phase Bias LRTI80	$\phi_t - \phi_r$
HH-VV Phase Slope LRTI80	$b_{\phi_t + \phi_r}$
HV-VH Phase Bias LRTI80	0

Using these calibration parameters we then re-process the Rosamond lines to estimate the quality of the calibration. In Figure (4) we show a typical plot of the data after calibration.

3 Cross-Talk Calibration

We use the radiometric and phase calibration parameters in the processor to produce data which has had radiometric and phase calibration applied. We then use this partially calibrated data as the input to the cross-talk calibration software. This provides a simple way to exclude cross-talk calibration if desired while still maintaining radiometric and phase calibration. We use the following distortion model [5, 1] to relate our observed scattering matrix elements (vector O) to the actual scattering matrix elements (vector S)

$$\begin{pmatrix} O_{hh} \\ O_{vh} \\ O_{hv} \\ O_{vv} \end{pmatrix} = Y \begin{pmatrix} 1 & w & v & vw \\ u & 1 & uv & v \\ z & wz & 1 & w \\ uz & z & u & 1 \end{pmatrix} \begin{pmatrix} \alpha & 0 & 0 & 0 \\ 0 & \alpha & 0 & 0 \\ 0 & 0 & 1 & 0 \\ 0 & 0 & 0 & 1 \end{pmatrix} \begin{pmatrix} k^2 & 0 & 0 & 0 \\ 0 & k & 0 & 0 \\ 0 & 0 & k & 0 \\ 0 & 0 & 0 & 1 \end{pmatrix} \begin{pmatrix} S_{hh} \\ S_{vh} \\ S_{hv} \\ S_{vv} \end{pmatrix} + \begin{pmatrix} N_{hh} \\ N_{vh} \\ N_{hv} \\ N_{vv} \end{pmatrix}. \quad (4)$$

Here, Y is a complex number, (u, v, w, z) are the complex cross-talk parameters (assumed to be small compared to 1), (k, α) are the co-pol channel imbalance and cross-pol channel imbalance respectively (assumed to be on the order of 1), and \vec{N} represents noise.

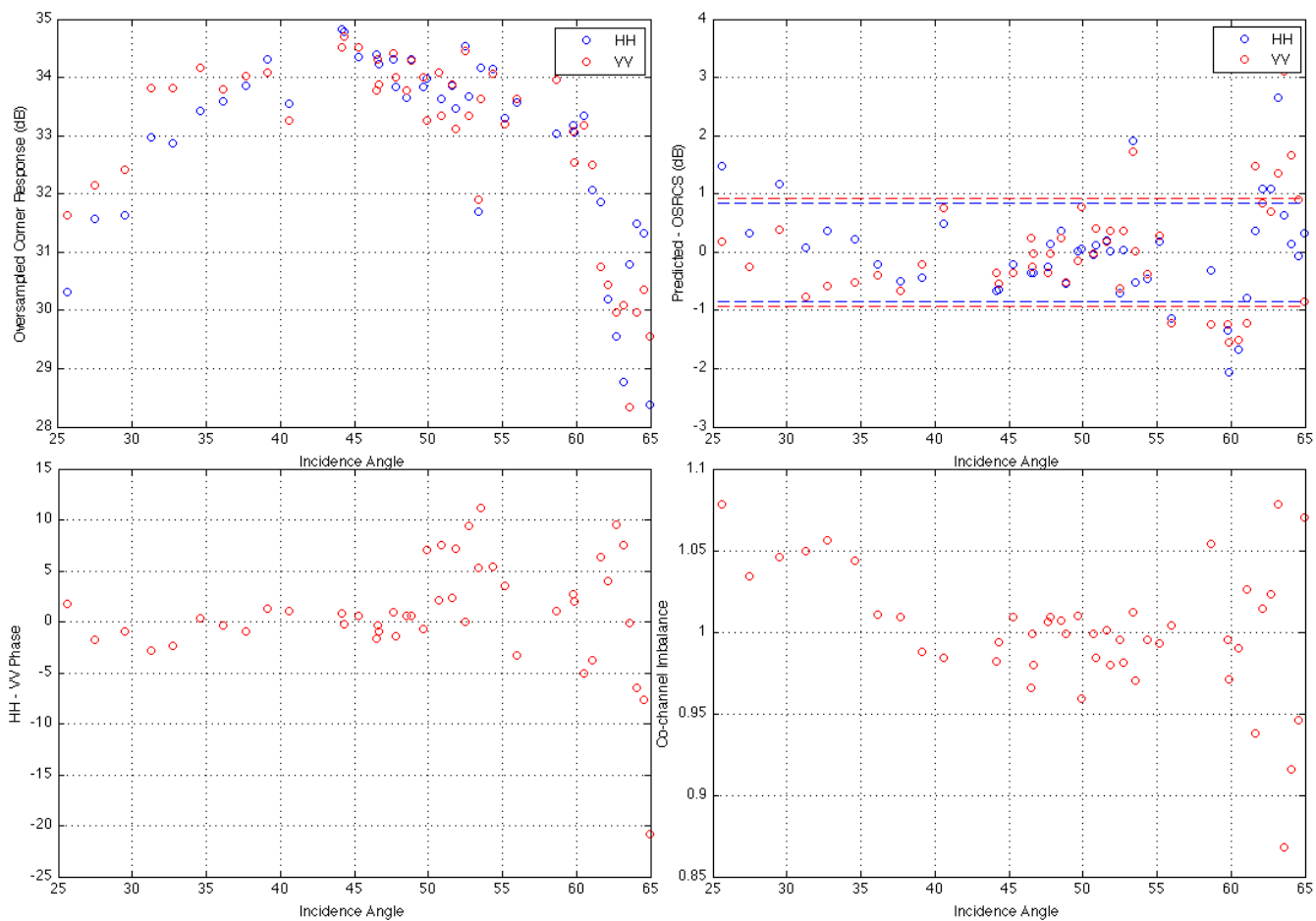


Figure 4: Data after re-processing using the calibration parameters estimated from Figure (1). The dashed lines in the upper right plot are drawn at \pm the standard deviation (≈ 1 dB) of the predicted RCS minus the measured RCS.

3.1 Algorithm

We assume that the data is already calibrated for radiometric and co-pol channel imbalance, as described in Section (2), therefore we set $Y = 1$ and $k = 1/\sqrt{\alpha}$. The system model then takes the form

$$\begin{pmatrix} O_{hh} \\ O_{vh} \\ O_{hv} \\ O_{vv} \end{pmatrix} = \mathbf{D} \begin{pmatrix} S_{hh} \\ S_{vh} \\ S_{hv} \\ S_{vv} \end{pmatrix} + \begin{pmatrix} N_{hh} \\ N_{vh} \\ N_{hv} \\ N_{vv} \end{pmatrix}, \quad (5)$$

where

$$\mathbf{D} = \begin{pmatrix} 1 & w\sqrt{\alpha} & v/\sqrt{\alpha} & vw \\ u & \sqrt{\alpha} & uv/\sqrt{\alpha} & v \\ z & wz\sqrt{\alpha} & 1/\sqrt{\alpha} & w \\ uz & z\sqrt{\alpha} & u/\sqrt{\alpha} & 1 \end{pmatrix} \quad (6)$$

is the distortion matrix. This system of equations has the solution

$$\begin{pmatrix} S_{hh} \\ S_{vh} \\ S_{hv} \\ S_{vv} \end{pmatrix} = \mathbf{\Sigma} \left[\begin{pmatrix} O_{hh} \\ O_{vh} \\ O_{hv} \\ O_{vv} \end{pmatrix} - \begin{pmatrix} N_{hh} \\ N_{vh} \\ N_{hv} \\ N_{vv} \end{pmatrix} \right]. \quad (7)$$

where

$$\mathbf{\Sigma} = \mathbf{D}^{-1} = \frac{1}{(uw-1)(vz-1)} \begin{pmatrix} 1 & -w & -v & vw \\ -u/\sqrt{\alpha} & 1/\sqrt{\alpha} & uv/\sqrt{\alpha} & -v/\sqrt{\alpha} \\ -z\sqrt{\alpha} & wz\sqrt{\alpha} & \sqrt{\alpha} & -w\sqrt{\alpha} \\ uz & -z & -u & 1 \end{pmatrix}, \quad (8)$$

is the calibration matrix. Note that the only assumptions made to simplify the distortion model is that the data has already had radiometric and co-pol channel imbalance calibration performed.

We use an algorithm similar to methods described in [5, 1]. We select a region of the image and compute the complex covariance matrix $C_{ij}^0 = \langle O_i O_j^* \rangle$ where the superscript * denotes the complex conjugate. From the covariance matrix, we estimate the cross-talk parameters as

$$\begin{aligned} u_0 &= (C_{44}^0 C_{21}^0 - C_{41}^0 C_{24}^0) / \Delta_0, \\ v_0 &= (C_{11}^0 C_{24}^0 - C_{21}^0 C_{14}^0) / \Delta_0, \\ z_0 &= (C_{44}^0 C_{31}^0 - C_{41}^0 C_{34}^0) / \Delta_0, \\ w_0 &= (C_{11}^0 C_{34}^0 - C_{31}^0 C_{14}^0) / \Delta_0, \end{aligned} \quad (9)$$

where $\Delta_0 = C_{11}^0 C_{44}^0 - |C_{14}^0|^2$. Note that these equations were derived in [5] by neglecting terms of order $\mathcal{O}(u, v, w, z)^2$. The cross-pol channel imbalance is estimated as

$$\alpha_0 = \frac{|\alpha_{0,1}\alpha_{0,2}| - 1 + \sqrt{(|\alpha_{0,1}\alpha_{0,2}| - 1)^2 + 4 + |\alpha_{0,2}|^2}}{2|\alpha_{0,2}|} \frac{\alpha_{0,1}}{|\alpha_{0,1}|}, \quad (10)$$

where

$$\begin{aligned} \alpha_{0,1} &= \frac{C_{22}^0 - u_0 C_{12}^0 - v_0 C_{42}^0}{X_0}, \\ \alpha_{0,2} &= \frac{X_0^*}{C_{33}^0 - z_0^* C_{31}^0 - w^* C_{34}^0}, \\ X_0 &= C_{32}^0 - z_0 C_{12}^0 - w_0 C_{42}^0. \end{aligned} \quad (11)$$

With these estimates we can compute the calibration matrix $\mathbf{\Sigma}_0$, and an estimate of the calibrated covariance matrix as $\mathbf{C}^1 := \mathbf{\Sigma}_0 \mathbf{C}^0 \mathbf{\Sigma}_0^\dagger$, where \dagger is the complex conjugate transpose operation.

3.2 Estimation of Cross-Talk Parameters

We estimate the cross-talk parameters u, v, w, z, α as a function of range. For every line of constant range we compute the covariance matrix C^0 for a “stripe” of pixels that lie within 10 samples of the current range-line. For every pixel included in this “stripe” of the image, we compute the $HH - HV$ correlation in a 5 by 5 pixel box centered on this pixel. If the $HH - HV$ correlation is greater than 0.2 we exclude this pixel from the covariance computation. We then use these covariance matrices to estimate the cross-talk parameters for each range-line. Next we apply a 100 sample moving window average to each of the cross-talk parameters, and then we generate and apply the calibration matrix Σ to the observed scattering matrix elements.

3.3 Range Dependence of Cross-Talk Parameters

In Figure (5) we plot our estimates of the cross-talk parameters estimated with the algorithm described in Section (3.1). In blue are the estimates of $10\log_{10}|u|, \arg(u)$ (top row), $10\log_{10}|v|, \arg(v)$ (2nd from top), $10\log_{10}|w|, \arg(w)$ (middle row), $10\log_{10}|z|, \arg(z)$ (2nd from bottom), and $|\alpha|, \arg(\alpha)$ (bottom row). We see generally that the cross-talk remaining in the data after correction is significantly lower than the cross-talk in the data before cross-talk calibration.

Note that the leaked power is proportional to the cross-talk parameters squared, so before cross-talk calibration the cross-talk of the system is on the order of -20 dB and after cross-talk calibration it is on the order of -35 to -40 dB.

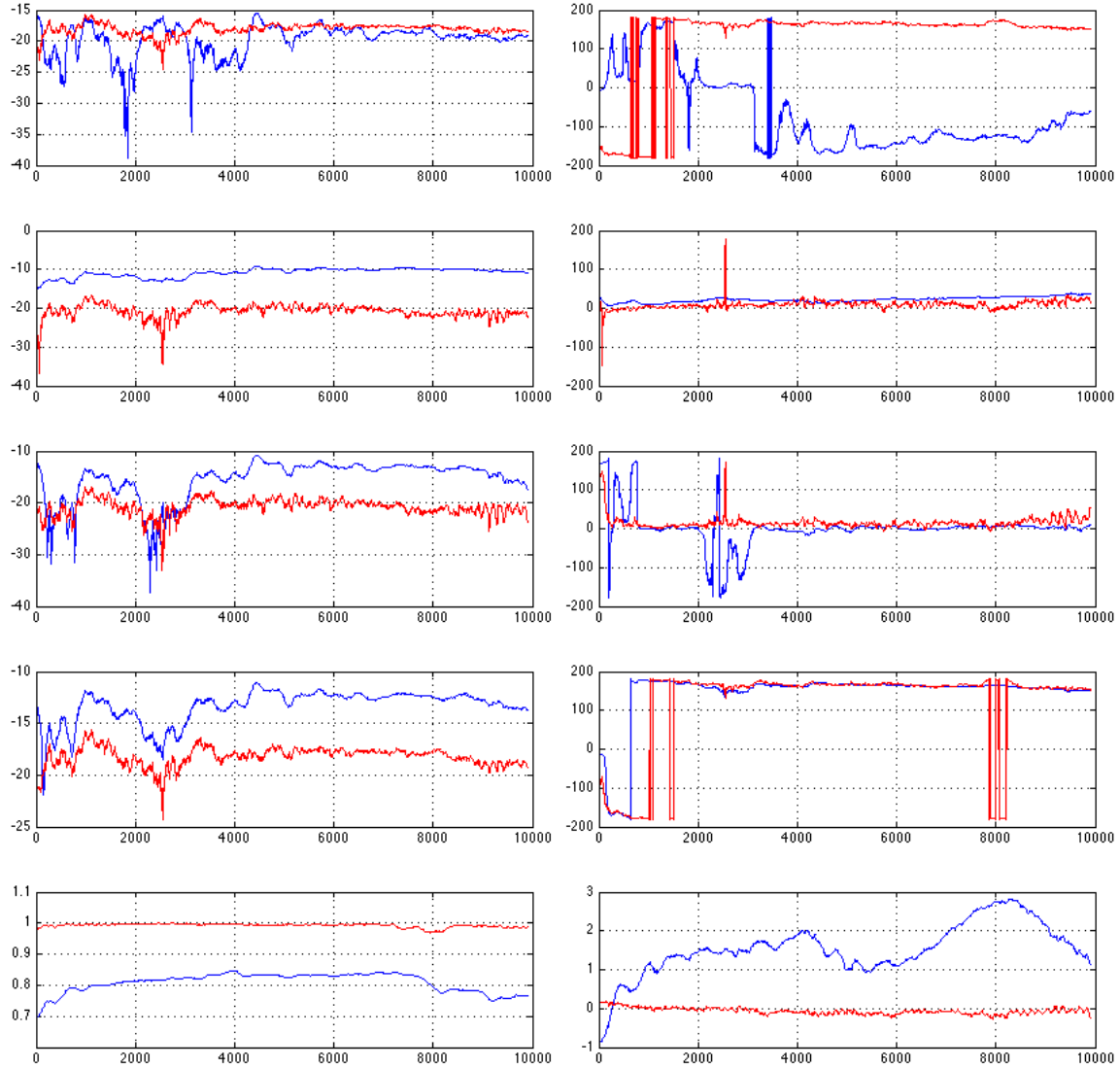


Figure 5: Cross-Talk parameters vs range for data from the flight over Rosamond (flight 38 line 35012). From the top down on the left we plot $|u|, |v|, |w|, |z|$ (dB) and $|\alpha|$, on the right we plot the corresponding phases in deg. In red are the values after cross-talk calibration and in blue are the values before cross-talk calibration.

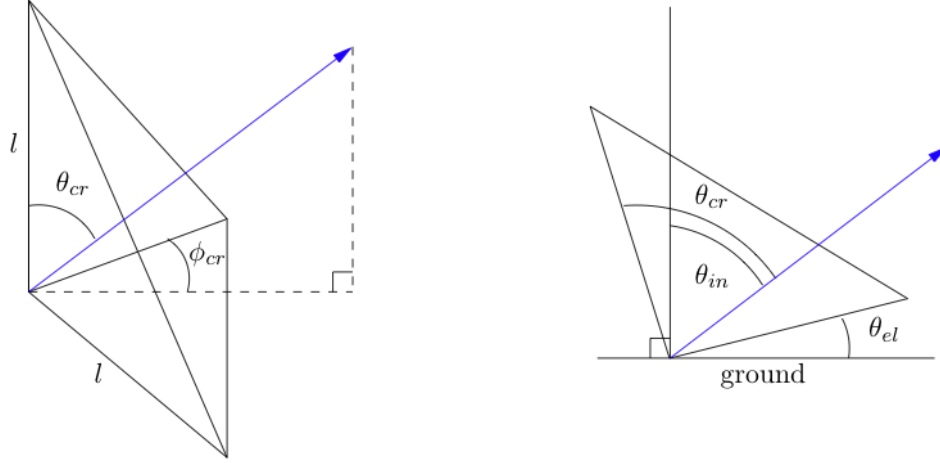


Figure 6: Diagrams of a trihedral corner reflector where the vector (blue) points towards the UAVSAR aircraft imaging pod. The incidence angle relative to the corner reflector, $\theta_{cr} := \theta_{in} + \theta_{el}$, where θ_{in} is the incidence angle, and θ_{el} is the elevation of the corner reflector relative to the ground. ϕ_{cr} is the azimuth angle relative to one of the vertical sides of the corner reflector. The maximum response of the corner reflector is for $\phi_{cr} = 45$ deg and $\theta_{cr} = 54.736$ deg.

A Corner Reflector Model

The theoretical radar cross section for a trihedral corner reflector is given by [2]

$$\sigma_{cr} = \frac{4\pi l^4}{\lambda^2} \left[\cos \theta_{cr} + \sin \theta_{cr} (\sin \phi_{cr} + \cos \phi_{cr}) - \frac{2}{\cos \theta_{cr} + \sin \theta_{cr} (\sin \phi_{cr} + \cos \phi_{cr})} \right]^2. \quad (12)$$

Here, $l = 2.4$ m is the length of the short sides of the corner reflector, $\lambda = 23.84$ cm is the radar wavelength, θ is the incidence angle relative to the corner reflector (i.e. the incidence angle plus the elevation angle of the corner reflector), and ϕ is the azimuth angle. If we introduce the vector \hat{P} which points from the imaging platform (plane) to the corner reflector, and the vector \hat{n} which points in the direction of bore sight of the corner reflector we can rewrite Eq. (12) as

$$\sigma_{cr} = \frac{4\pi l^4}{\lambda^2} \left[\sqrt{3} \hat{P} \cdot \hat{n} - \frac{2}{\sqrt{3} \hat{P} \cdot \hat{n}} \right]^2. \quad (13)$$

B Antenna Pattern

UAVSAR uses an electronically steered 48 element antenna with 12 columns of elements in the \hat{e} direction and 4 rows of elements in the \hat{d} direction (see Figure (7(a))). The two outer rows of elements in the \hat{d} direction are reduced in amplitude by $a_2 = 0.316$ relative to the two inner rows while no taper is applied in the \hat{e} direction. The antenna pattern has the following analytic expression [4]:

$$g(\alpha, \epsilon, \alpha_0) = \frac{(\cos \alpha \cos \epsilon)^{1.5}}{1 + a_2} \text{sinc} \left[\frac{\pi L_e}{\lambda} (\sin \alpha - \sin \alpha_0) \right] \left\{ \cos \left[\frac{\pi L_{d1}}{\lambda} (\cos \alpha \sin \epsilon) \right] + a_2 \cos \left[\frac{\pi L_{d2}}{\lambda} (\cos \alpha \sin \epsilon) \right] \right\}. \quad (14)$$

Here, $\lambda = 0.238$ meters is the wavelength, α is the antenna azimuth angle, ϵ is the antenna elevation angle, α_0 is the antenna azimuth angle to which we electronically steer the antenna array, $L_e = 1.5$ meters is the antenna length in the \hat{e} direction, $L_{d1} = 0.1$ meters is the spacing between the two inner rows of the antenna array, and $L_{d2} = 0.3$ meters is the spacing between the two outer rows of the antenna array.

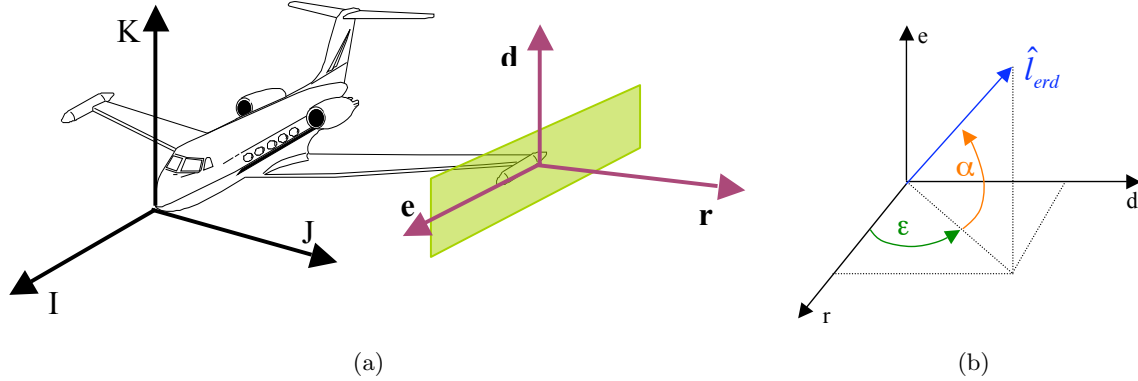


Figure 7: In Figure (7(a)) we show a diagram of the UAVSAR antenna geometry and antenna-face coordinates. Note that the antenna is actually mounted to the aircraft with an additional rotation about the \hat{I} direction of -45 deg. In Figure (7(b)) we show the definition of the elevation ϵ and azimuth α directions. Figures are from [4].

During processing of UAVSAR imagery the processor applies an antenna pattern correction based on Eq. (14), however it has been slightly modified to improve agreement with near-field range measurements of the UAVSAR antenna [3]. In Figures (8-9) we plot a comparison of the model antenna pattern to range measurements of the UAVSAR antenna. We see that the modified model antenna pattern matches very well (difference less than 1 dB) to the measured antenna pattern for elevation in the range of $[-20, 20]$ deg. In Figure (10) we plot the two-way HH and VV gains for azimuth and elevation cuts across boresight for $\theta_{esa} = \{-25, 0, 25\}$ deg. We can clearly see the shift of bore-sight due to the electronic steering in the azimuth patterns, and very little change in the elevation patterns. In Figure (11) we plot the two-way -3 dB azimuth and elevation beam widths as a function of θ_{esa} . We see that the elevation and azimuth beam-widths only vary on the order of 1 degree over the range of electronic scanning angles.

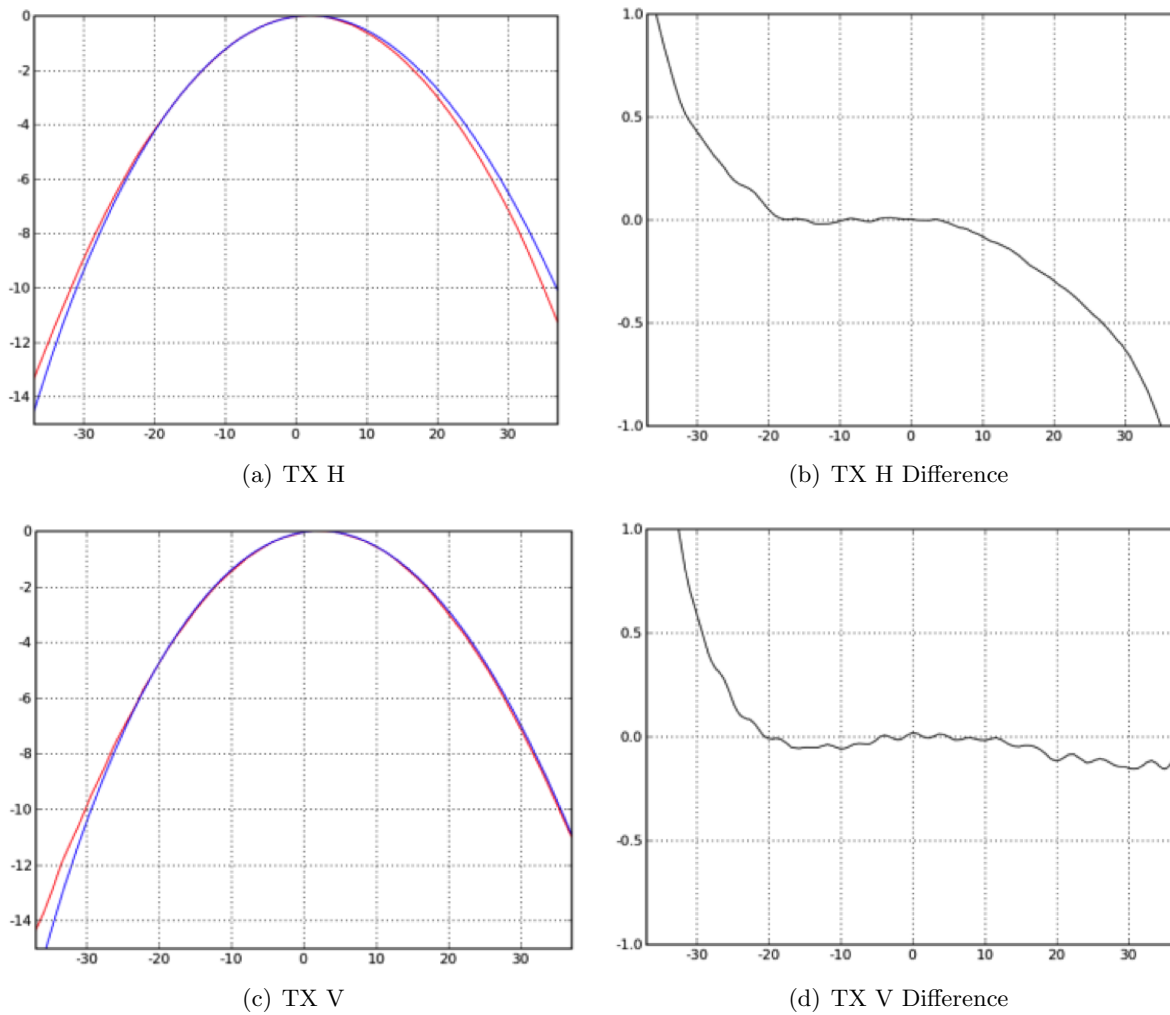


Figure 8: Comparison of modified UAVSAR antenna pattern used in processor to range measurements of the UAVSAR antenna. On the left the model antenna patterns are plotted in blue, the measured pattern is plotted in red, and they are plotted in dB as a function of elevation. On the right is the measured antenna pattern minus the model antenna pattern. In every case for elevation between -20 deg and 20 deg the difference is less than 1 dB. Figures are from [3].

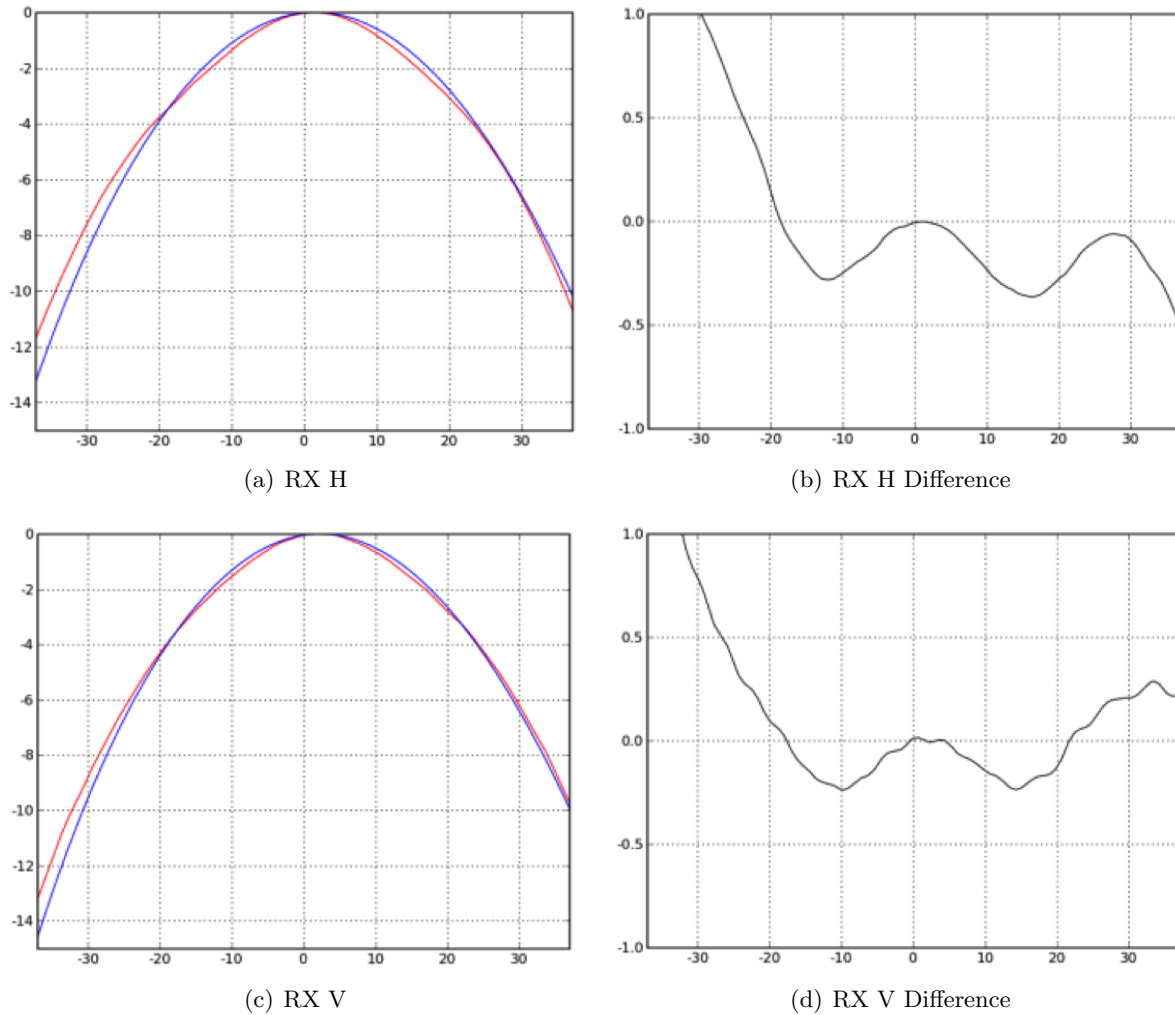


Figure 9: Comparison of modified UAVSAR antenna pattern used in processor to range measurements of the UAVSAR antenna. On the left the model antenna patterns are plotted in blue, the measured pattern is plotted in red, and they are plotted in dB as a function of elevation. On the right is the measured antenna pattern minus the model antenna pattern. In every case for elevation between -20 deg and 20 deg the difference is less than 1 dB. Figures are from [3].

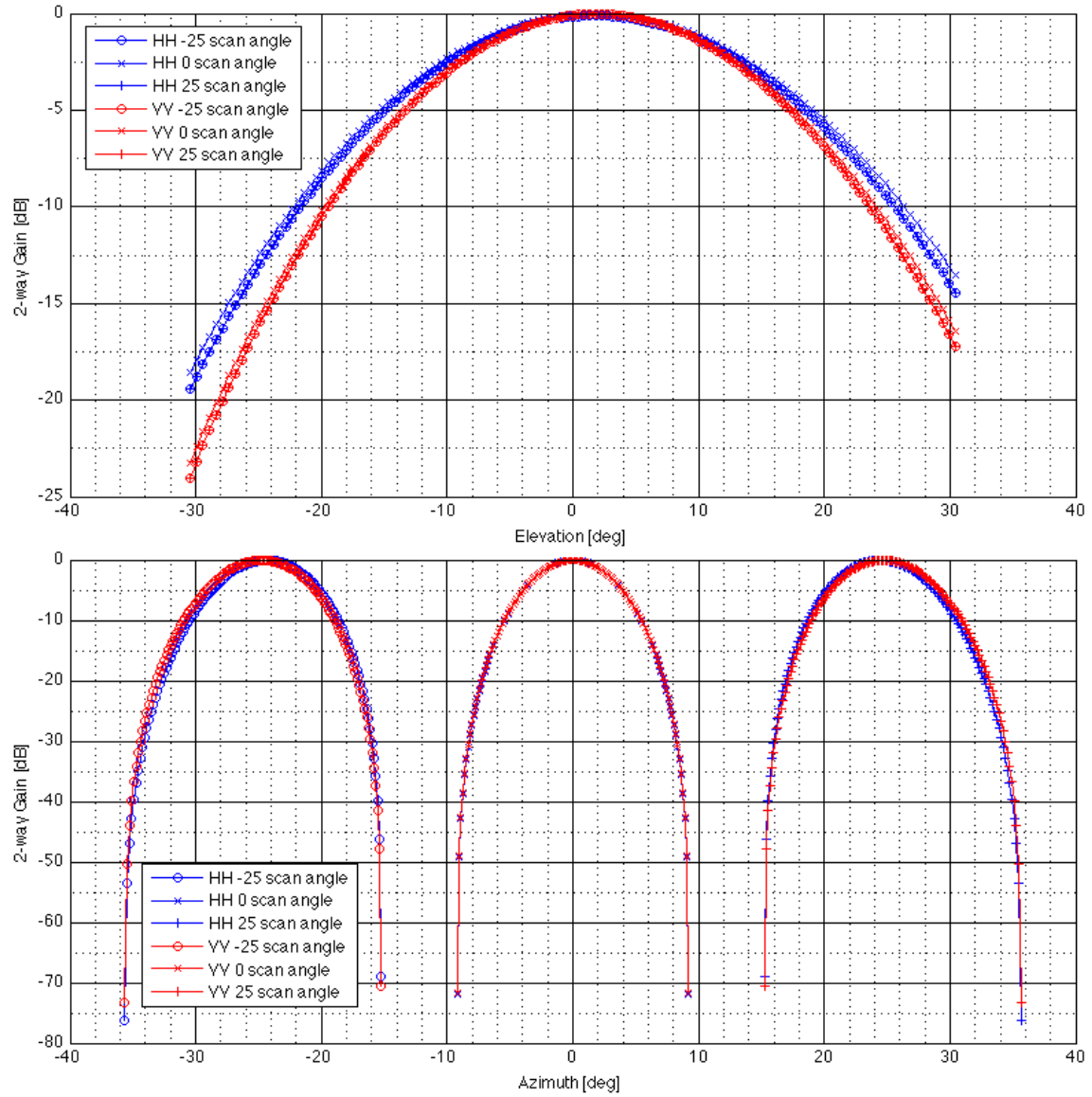


Figure 10: Modified UAVSAR model antenna patterns for different electronic steering angles. We plot cuts across bore-sight in elevation and azimuth for $\theta_{esa} = \{-25, 0, 25\}$ deg.

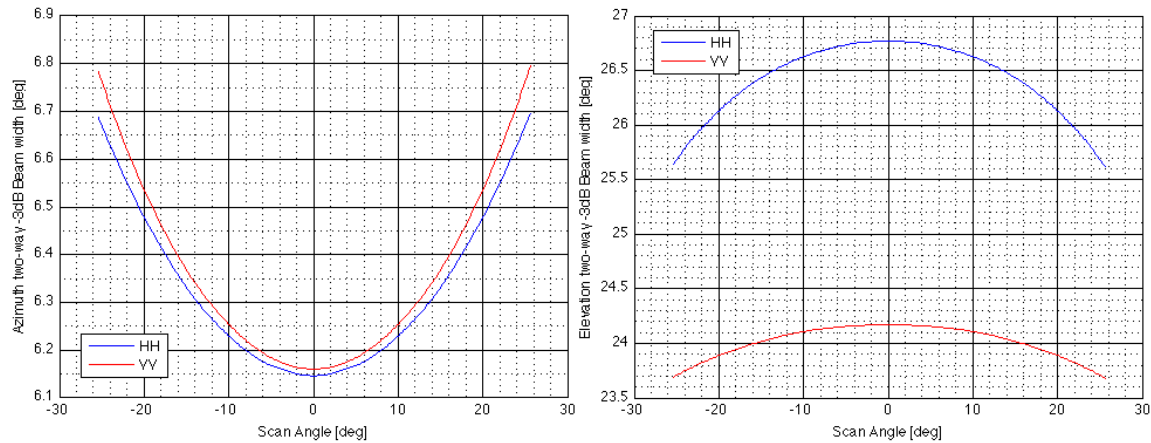


Figure 11: Modified UAVSAR model antenna pattern two-way -3 dB beam widths in the azimuth and elevation directions as a function of the electronic steering angle. Over the range of electronic steering angles the variation of the beam-widths is on the order of 1 degree.

References

- [1] T.L. Ainsworth, L. Ferro-Famil, and Jong-Sen Lee. Orientation angle preserving a posteriori polarimetric sar calibration. *IEEE Transactions on Geoscience and Remote Sensing*, 44(4):994–1003, April 2006.
- [2] R R Bonkowski, Lubitz C R, and Schensted C E. Studies in radar cross-sections - vi. cross-sections of corner reflectors and other multiple scatterers at microwave frequencies. Technical report, University of Michigan Radiation Laboratory, <http://hdl.handle.net/2027.42/21139>, October 1953.
- [3] Mauro Grando and Greg Sadowy. Simulated uavsar patterns matched to measured patterns. Interoffice Memorandum, August 2008.
- [4] Scott Hensley and Marc Simard. Antenna coordinates, look vector computations and imaging time estimation. Interoffice Memorandum, August 2006.
- [5] S. Quegan. A unified algorithm for phase and cross-talk calibration of polarimetric data-theory and observations. *IEEE Transactions on Geoscience and Remote Sensing*, 32(1):89–99, Jan 1994.
- [6] J.J. van Zyl, Charles F. Burnette, Howard A. Zebker, Anthony Freeman, and John Holt. Polcal user's manual, August 1992.